PROCEEDINGS OF THE ROYAL SOCIETY A MATHEMATICAL, PHYSICAL & ENGINEERING SCIENCES

Detecting the mass and position of an adsorbate on a drum resonator

Y. Zhang and Y. P. Zhao

Proc. R. Soc. A 2014 **470**, 20140418, published 30 July 2014

PROCEEDINGS OF THE ROYAL SOCIETY A

rspa.royalsocietypublishing.org

Detecting the mass and position of an adsorbate on a drum resonator

Y. Zhang and Y. P. Zhao

State Key Laboratory of Nonlinear Mechanics (LNM), Institute of Mechanics, Chinese Academy of Sciences, Beijing 100190, People's Republic of China

Research

Cite this article: Zhang Y, Zhao YP. 2014 Detecting the mass and position of an adsorbate on a drum resonator. *Proc. R. Soc. A* **470**: 20140418.
http://dx.doi.org/10.1098/rspa.2014.0418

Received: 25 May 2014
Accepted: 30 June 2014

Subject Areas:
mechanics, nanotechnology

Keywords:
circular membrane, resonant frequencies, resonator sensor, inverse problem, graphene

Author for correspondence:
Y. Zhang
e-mail: zhangyin@lnm.imech.ac.cn

The resonant frequency shifts of a circular membrane caused by an adsorbate are the sensing mechanism for a drum resonator. The adsorbate mass and position are the two major (unknown) parameters determining the resonant frequency shifts. There are infinite combinations of mass and position which can cause the same shift of one resonant frequency. Finding the mass and position of an adsorbate from the experimentally measured resonant frequencies forms an inverse problem. This study presents a straightforward method to determine the adsorbate mass and position by using the changes of two resonant frequencies. Because detecting the position of an adsorbate can be extremely difficult, especially when the adsorbate is as small as an atom or a molecule, this new inverse problem-solving method should be of some help to the mass resonator sensor application of detecting a single adsorbate. How to apply this method to the case of multiple adsorbates is also discussed.

1. Introduction

The ultimate goal of any detection method is to achieve the level of resolving a single quantum of a measured entity [1]. To pursue this goal, various mechanisms are used. For example, the presence of a single NO_2 molecule on graphene is detected by measuring the Hall resistivity change during the adsorption and desorption processes [1]; a single biotin–streptavidin binding on a nanowire is detected by measuring the conductance change [2]; a single biotin–streptavidin binding on a nanorod is also detected by measuring the shift of its surface plasmon resonance [3]. As for an inertial mass resonator, the resonance frequency shift owing to the adsorption/binding of a particle is the

detecting mechanism. The ultimate limit for the mass resonator sensitivity is imposed by the thermodynamic fluctuation [4,5], which has been theoretically proved to be well below a single dalton (1 dalton $\approx 1.65 \times 10^{-24}$ g is the mass of a proton) [5]. Enormous efforts have been made to push the mass resonator sensitivity towards the limit. There are three major approaches to enhance the mass resonator sensitivity. Because the resonant frequency of a beam is proportional to $h/L^2 \times \sqrt{E/\rho}$ (h and L are the thickness and length; E and ρ are the Young modulus and mass density) [6–8], the first is to scale down the structure size, which makes the factor of h/L^2 larger and at the same time the fractional change in mass is also larger in a smaller resonator for the same adsorbate. The second is to use the materials with large E/ρ, such as carbon nanotube (CNT) [9–11], graphene [7] and silicon carbide [12]. Both approaches result in higher resonant frequencies. Therefore, a small fractional change in resonant frequency is still absolutely large enough to be detected [13]. As a two-dimensional material, the monolayer graphene has reached the limit of the scaling-down strategy and has its whole volume exposed to surface adsorbates [1]. At the same time, the very small interstitial space owing to the close packing of carbon atoms in graphene does not allow small atoms such as helium to pass through [14]. This impermeability property, which makes the adsorption of small atoms possible, is a necessity for pushing the sensitivity of a graphene mass resonator towards the limit. Graphene is also the strongest material ever tested [15], which can take the failure strain up to 12%. The large tensile in-plane stress inside a suspended graphene, which can be applied or simply result from the uncontrolled forces applied during the exfoliation process [16], can further increase the resonant frequency. Sometimes, the binding between an adsorbate and graphene/CNT is not strong enough to prevent the adsorbate diffusion [17,18]. The adsorbate movement can be a significant source of noise and error in the measurement of the mass resonator [17]. The presence of large tensile stress can significantly reduce or suppress the adsorbate movement [18]. Unlike the above two approaches, which in essence increase resonant frequency, the third one is to increase the quality factor. The quality factor (Q) determines the 'sharpness' of the resonance, which is inversely proportional to damping and is approximately given as [19]

$$Q = \frac{1.09 f_o}{\Delta f}, \tag{1.1}$$

where f_o is the resonant frequency and Δf is its shift. Clearly, for a given resonant frequency, larger Q means that smaller Δf can be detected. Although various models and mechanisms are proposed [20,21], a clear picture of the quality factor variation of small-scale structures still remains elusive [21]. The in-plane tension is shown to increase the quality factor significantly by both simulation [18] and experiment [22]. It is always effective to increase the quality factor by putting the mass resonator in a vacuum environment, which reduces or eliminates the damping owing to ambient air [23]. A quality factor as large as 100 000 has been achieved in a graphene resonator [19].

The sensitivity of micro/nanomechanical mass resonators has been steadily improving with roughly an order of magnitude per year [4]. Hanay *et al.* [24] used silicon-based nanoelectromechanical systems technology to develop a mass resonator capable of detecting a single protein with a mass of around 1 million dalton (MDa); Jensen *et al.* [9] developed a CNT-based mass resonator with the capability of detecting a single gold atom with a mass of 196.967 Da; Chiu *et al.* [10] developed a CNT-based mass resonator capable of detecting a single xenon atom (131.293 Da) and a single argon atom (39.948 Da). Sensitivity for detecting a 1 Da mass has recently been achieved by Chaste *et al.* [11] in their CNT-based mass resonator. Although these achievements are very impressive, there is a fundamental problem remaining in these mass resonators: all the frequency shift measurements actually cannot give the mass of an individual atom, molecule or nanoparticle [24]. As demonstrated by Jensen *et al.* [9], their CNT-based mass resonator actually does not measure the mass of a gold atom even though the resonator has the capability of detecting a smaller frequency shift induced by the adsorption of a gold atom. The atom/molecule/particle mass and its position are the two (major) convolving factors of determining the resonant frequency shift of a resonator. To know the position, there

are three major experimental approaches: (i) measuring the trajectory of a sprayed particle [4]; (ii) occluding some portions of resonator so that the particle must land at a specific location [9]; and (iii) direct measurement of the position of an adsorbate [25]. These measurement approaches not only require extra experimental set-up, but also (sometimes) are extremely difficult if not impossible to be applied. For example, Dohn *et al.* [25] determined the position of a micrometre-sized particle by using optical imaging. However, in the resonator described by Burg *et al.* [26] that had an embedded microfluidic channel where the biomolecules are pumped in, the optical method did not work, because of the smaller size of a biomolecule and the small contrast between a biomolecule and solution. The exact position of the biomolecule is thus a major uncertainty in this experiment [26]. The following insightful comment by Knobel [13] fully summarizes the motivation of this study: before a practical mechanical mass spectrometer can be made, the most important problem to be solved is to determine the atom/molecule/particle position.

In this study, we present a method to determine the mass and position of an adsorbate on a circular resonator, which is also often referred to as a drum resonator [27–29]. In a forward problem, the adsorbate mass and position are given to calculate the resonant frequency [30–34]. However, in the real application of a mass resonator, resonant frequencies are the measured quantities; the adsorbate mass and position are the unknowns to be determined [35]. An inverse problem is thus encountered: how can we use the measured resonant frequencies to determine the adsorbate mass and position? This inverse problem is solved based on the following two mechanisms: (i) the adsorbate mass and position have different impacts on the same resonant frequency and (ii) for a circular membrane that has infinite resonant frequencies, the same adsorbate mass and position have different impacts on different resonant frequencies [25]. In essence, we use two resonant frequencies to uniquely determine the adsorbate mass and position. The methods of using multiple resonant frequencies to determine the mass and position of a single adsorbate have been developed [24,36]. However, unlike the method of probability density function [24] or a minimizing procedure which requires at least four resonant frequencies to be measured [36], this study presents a straightforward method to attack this inverse problem and its accuracy is also demonstrated.

2. Model development

Figure 1*a* is a schematic of a graphene layer deposited on a circular hole with radius r_a. Figure 1*b* shows the polar coordinate system and an adsorbate is located at (r_o, θ_o). The membrane potential energy, U, is given as follows:

$$U = \frac{F}{2}\int_0^{r_a}\int_0^{2\pi}\left[\left(\frac{\partial w}{\partial r}\right)^2 + \left(\frac{1}{r}\frac{\partial w}{\partial \theta}\right)^2\right] r\,\mathrm{d}r\,\mathrm{d}\theta, \tag{2.1}$$

where F is the tensile force per unit length at the boundary and w is the membrane displacement. The kinetic energy, T, is given as follows:

$$T = \frac{m}{2}\int_0^{r_a}\int_0^{2\pi}\left(\frac{\partial w}{\partial t}\right)^2 r\,\mathrm{d}r\,\mathrm{d}\theta + \frac{\Delta M}{2}\left(\frac{\partial w}{\partial t}\right)^2\Bigg|_{r=r_o,\theta=\theta_o}. \tag{2.2}$$

Here m is the membrane mass per unit area and $m = \rho h$ (ρ, h are the mass density and thickness, respectively). ΔM is the adsorbate mass and $\partial w/\partial t|_{r=r_o,\theta=\theta_o}$ is the corresponding velocity at (r_o, θ_o). Here, the effect of an adsorbate is modelled as a concentrated mass [32–34]. To write down the above expressions for the potential and kinetic energies, the following five assumptions are used. (i) The continuum modelling applies to graphene, which is corroborated by the atomistic studies of the monolayer graphene [37,38]. (ii) The potential energy of equation (2.1) does not include the bending energy, which is another way of saying that the suspended graphene is modelled as a membrane structure. The atomistic simulation shows that monolayer graphene has a bending stiffness close to that of a lipid bilayer of a cell [37], which may have some potential in biological application. Because of large applied or residual in-plane tension, the potential energy owing

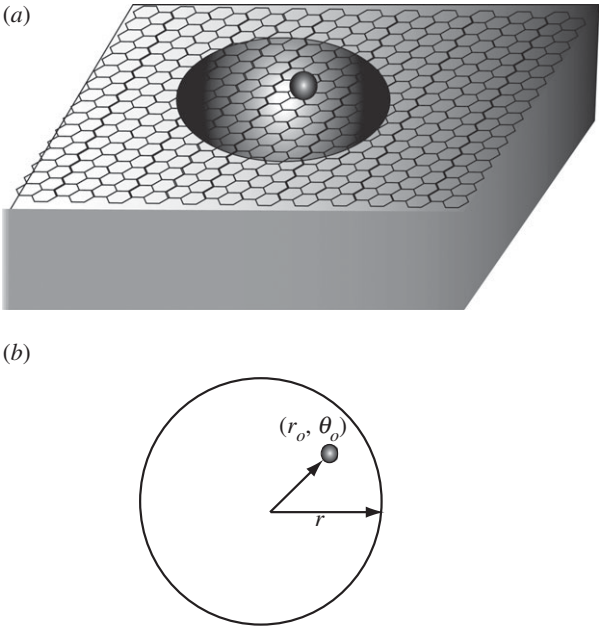

Figure 1. (*a*) Schematic of a graphene layer deposited on a substrate with a circular hole. (*b*) The polar coordinate system. The circle radius is r_a and an adsorbate is located at (r_o, θ_o).

to tension is often several orders of magnitude larger than the bending energy [15]. With the presence of large in-plane tension, a plate structure behaves like a membrane one [39]. Therefore, the suspended graphene is often modelled as a membrane structure [15,22,27–29,31,40–42]. (iii) Equation (2.1) does not include the potential energy contributions induced by an adsorbate or heating by assuming that the pre-existing in-plane tension is very large compared with those induced by adsorbate or heating. Because of the adsorption-induced electronic and mechanical distortion of a graphene structure [43,44], an adsorbate can impart a tension to a suspended graphene, which causes the increase in resonant frequency [42]. At the same time, a suspended graphene is often actuated by laser heating [22,27–29], which induces thermal stress and thus changes the in-plane tension. The in-plane tension inside a graphene is quite often remarkably high and higher than the fracture strength of most materials [15,18]. Besides advantages such as reducing adsorbate diffusion, and increasing resonant frequencies and the quality factor as mentioned above [18,22], the presence of large in-plane tension also has other advantages. For example, the suspended graphene is usually non-flat with ripples [42], which causes local elastic distortion and thus complicates our analysis. Also, tension or heating (keeping in mind that graphene has negative thermal expansion coefficient) can reduce or suppress the ripples [41]. Another advantage is associated with the following fourth assumption. (iv) The geometric nonlinearity owing to large deflection is not considered. When the deflection amplitude is (very) large, the nonlinear Duffing equation becomes the governing equation [31,42], which, again, can further complicate our analysis. The presence of in-plane tension can delay the onset of nonlinearity, which is to say that the system stays in a linear range even when the amplitude is relatively large [42]. (v) Because r_a is the radius of a hole on a substrate, the assumption here is that no peeling-off occurs. When a graphene sheet is deposited on a substrate, adhesion is responsible for the binding [40], which is induced by the van der Waals force [45]. With a large deflection amplitude, peeling-off can occur [46], which means that the actual radius of the graphene sheet is varying and larger than r_a. This moving boundary together with the induced degenerate modes as discussed later in detail can make the analysis extremely difficult. Koenig's experiment shows that the adhesion of graphene sheet is 'ultrastrong' [40], which together with the fourth assumption of small deflection ensures this no peeling-off assumption.

The following non-dimensionalization scheme is introduced:

$$\xi = \frac{r}{r_a}, \quad W = \frac{w}{r_a} \quad \text{and} \quad \xi_o = \frac{r_o}{r_a}. \tag{2.3}$$

Now the potential energy and kinetic energy become the following forms:

$$U = \frac{Fr_a^2}{2}\int_0^1\int_0^{2\pi}\left[\left(\frac{\partial W}{\partial \xi}\right)^2 + \left(\frac{1}{\xi}\frac{\partial W}{\partial \theta}\right)^2\right]\xi \, \mathrm{d}\xi \, \mathrm{d}\theta \tag{2.4}$$

and

$$T = \frac{mr_a^4}{2}\int_0^1\int_0^{2\pi}\left(\frac{\partial W}{\partial t}\right)^2 \xi \, \mathrm{d}\xi \, \mathrm{d}\theta + \frac{\Delta M r_a^2}{2}\left(\frac{\partial W}{\partial t}\right)^2\Bigg|_{\xi=\xi_o,\theta=\theta_o}. \tag{2.5}$$

Before we start to compute the resonant frequencies of the membrane with an adsorbate, we need to have a brief discussion on the membrane vibration pattern, which is important not only to the computation but also to the mass resonator application. By the method of separation of variables, W can be expressed as follows [47–49]:

$$W(\xi, \theta, t) = V(\xi, \theta)\cos(\omega t) = R(\xi)\Theta(\theta)\cos(\omega t), \tag{2.6}$$

where ω is the membrane resonant frequency/eigenfrequency; $V(\xi, \theta)$ is the spatial part, which is decomposed further into two parts, R and Θ. For a uniform membrane with no adsorbate, the governing equation is the following [47–49]:

$$m\frac{\partial^2 W}{\partial t^2} - F\bigtriangledown^2 W = 0, \tag{2.7}$$

where $\bigtriangledown^2$ is the Laplace operator defined as

$$\bigtriangledown^2 = \frac{\partial^2}{\partial r^2} + \frac{1}{r}\frac{\partial}{\partial r} + \frac{1}{r^2}\frac{\partial^2}{\partial \theta^2} = \frac{\partial^2}{a^2\partial \xi^2} + \frac{1}{a^2\xi}\frac{\partial}{\partial \xi} + \frac{1}{a^2\xi^2}\frac{\partial^2}{\partial \theta^2}. \tag{2.8}$$

By substituting equation (2.6) into equation (2.7), the Bessel equation is obtained, which is a classical problem and the detailed solution process can be found elsewhere [47–49]. Here we summarize only some of results, as follows [47,48]:

$$V(\xi, \theta) = R(\xi)\Theta(\theta) = \sum_{n=0}^{\infty}\sum_{i=1}^{\infty}[a_{ni}J_n(\lambda_{n,i}\xi)\cos(n\theta) + b_{ni}J_n(\lambda_{n,i}\xi)\sin(n\theta)], \tag{2.9}$$

where n and i are two positive integers; a_{ni} and b_{ni} are the (unknown) constants associated with the modes. J_n is the Bessel function of the first kind and $\lambda_{n,i}$ is the value corresponding to the ith zero of J_n. When $n \neq 0$, which is the so-called degenerate case [48], there are two modes at a resonant frequency: $J_n(\lambda_{n,i}\xi)\cos(n\theta)$ and $J_n(\lambda_{n,i}\xi)\sin(n\theta)$, which thus means that the linear combination of these two modes, i.e. $a_{ni}J_n(\lambda_{n,i}\xi)\cos(n\theta) + b_{ni}J_n(\lambda_{n,i}\xi)\sin(n\theta)$, is also the mode. When $n \neq 0$, the mode is θ-dependent and thus non-axisymmetric. Only when $n = 0$ can the corresponding modes be axisymmetric [47–49]. The three lowest axisymmetric mode shapes of $J_0(\lambda_{0,1}\xi)$, $J_0(\lambda_{0,2}\xi)$ and $J_0(\lambda_{0,3}\xi)$ with $\lambda_{0,1} = 2.4048$, $\lambda_{0,2} = 5.5201$ and $\lambda_{0,3} = 8.6537$ [50] and the three lowest non-axisymmetric modes of $J_1(\lambda_{1,1}\xi)\cos(\theta)$, $J_2(\lambda_{2,1}\xi)\cos(2\theta)$ and $J_3(\lambda_{3,1}\xi)\cos(3\theta)$ with $\lambda_{1,1} = 3.8317$, $\lambda_{2,1} = 5.1356$ and $\lambda_{3,1} = 6.3802$ [50] are plotted in figure 2. When those non-axisymmetric modes are excited, this θ-dependent property will make the detection of mass and its position much more difficult. In addition to the non-axisymmetric modes introducing another variable θ, the mode shape of $a_{ni}J_n(\lambda_{n,i}\xi)\cos(n\theta) + b_{ni}J_n(\lambda_{n,i}\xi)\sin(n\theta)$ also becomes dependent on the initial conditions, which can make the identification of resonance very difficult, because the resonant peak magnitude can change from time to time owing to the change of the initial conditions. As shown in the resonance spectrum of a circular graphene membrane in the experiment described by Barton *et al*. [29], multiple peaks cluster around their predicted resonant frequencies because of the presence of the degenerate modes. These non-axisymmetric

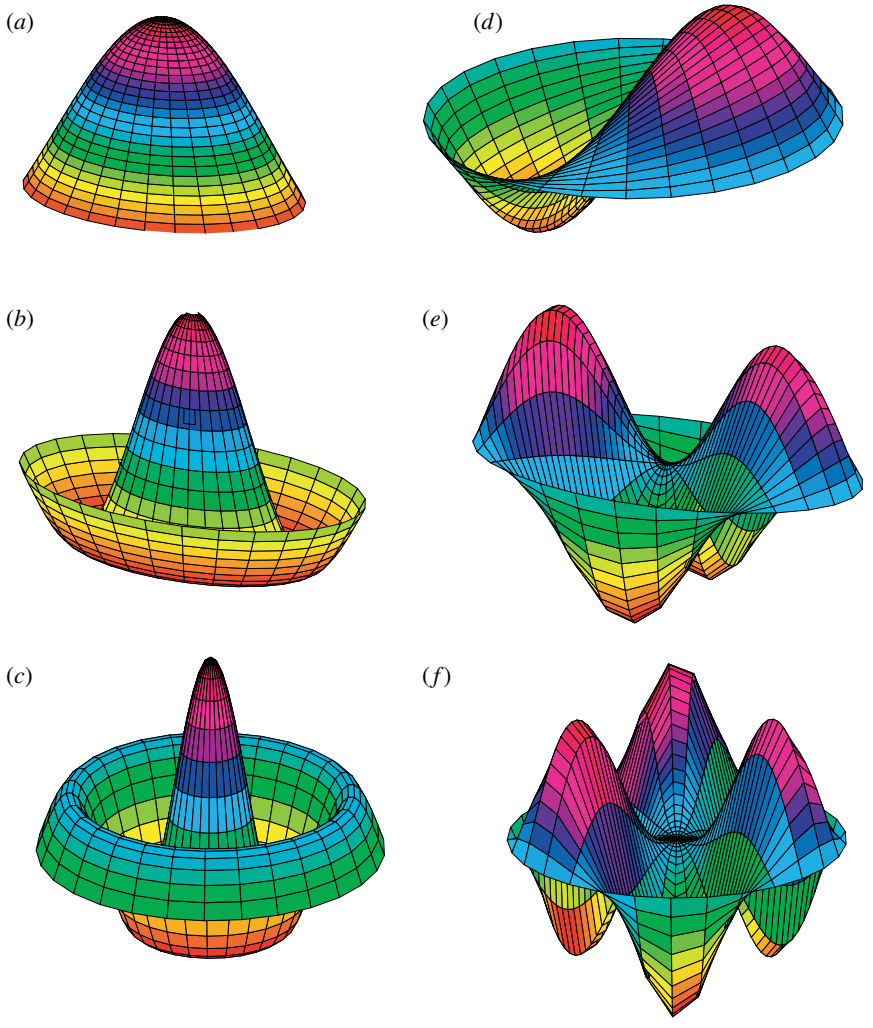

Figure 2. Axisymmetric and non-axisymmetric modes. (*a–c*) The axisymmetric modes of (*a*) $J_0(\lambda_{0,1}\xi)$, $\lambda_{0,1} = 2.4048$; (*b*) $J_0(\lambda_{0,2}\xi)$, $\lambda_{0,2} = 5.5201$; and (*c*) $J_0(\lambda_{0,3}\xi)$, $\lambda_{0,3} = 8.6537$. (*e–g*) The non-axisymmetric modes of (*d*) $J_1(\lambda_{1,1}\xi)\cos(\theta)$, $\lambda_{1,1} = 3.8317$; (*e*) $J_2(\lambda_{2,1}\xi)\cos(2\theta)$, $\lambda_{2,1} = 5.1356$; and (*f*) $J_3(\lambda_{3,1}\xi)\cos(3\theta)$, $\lambda_{3,1} = 6.3802$. (Online version in colour.)

degenerate modes are induced by the asymmetry caused by surface contamination [29]. In the application of the mass resonator sensor, these non-axisymmetric modes should be avoided. On the other hand, when the boundary is well defined [28], which means that no peeling-off occurs, the non-axisymmetric modes will not be excited as long as the membrane initial configuration and excitation force are axisymmetric [49]. Because of the presence of very large residual tensile stress, the graphene layer has a flat initial configuration and a spatially uniformly distributed pressure/load can be easily exerted, which can effectively prohibit the appearance of non-axisymmetric modes.

If only the axisymmetric modes are excited, equation (2.9) can now be written in a simpler form, as follows [47–49]:

$$V(\xi,\theta) = V(\xi) = \sum_{i=1}^{\infty} a_i J_0(\lambda_{0,i}\xi), \tag{2.10}$$

where a_i is the unknown constant associated with each mode. In the computation, only finite mode shapes are used. As shown later, we need to compute only the first two eigenfrequencies

and six modes in total are used, which is shown to be accurate enough. Correspondingly, the potential and kinetic energies associated with the axisymmetric deformation become the following:

$$U = \pi r_a^2 F \int_0^1 \left(\frac{\partial W}{\partial \xi}\right)^2 \xi \, \mathrm{d}\xi \tag{2.11}$$

and

$$T = \pi r_a^4 m \int_0^1 \left(\frac{\partial W}{\partial t}\right)^2 \xi \, \mathrm{d}\xi + \frac{\Delta M r_a^2}{2} \left(\frac{\partial W}{\partial t}\right)^2 \Bigg|_{\xi=\xi_o}. \tag{2.12}$$

By substituting equations (2.6) and (2.10) into equations (2.11) and (2.12), minimizing the functional $T - U$, i.e. $\partial(T-U)/\partial a_i = 0$ [49,51], leads to the following eigenvalue problem:

$$\mathbf{K} - \lambda^2 \mathbf{M} = 0, \tag{2.13}$$

where $\lambda = \sqrt{m r_a^2 \omega^2 / F}$ is the dimensionless eigenfrequency; $\mathbf{K}$ and $\mathbf{M}$ are the matrices defined as

$$\mathbf{K}_{ij} = \frac{\partial^2}{\partial a_i \partial a_j} \left[\int_0^1 \left(\frac{\mathrm{d}V}{\mathrm{d}\xi}\right)^2 \xi \, \mathrm{d}\xi\right] = \int_0^1 \frac{\mathrm{d}J_0(\lambda_{0,i}\xi)}{\mathrm{d}\xi} \times \frac{\mathrm{d}J_0(\lambda_{0,j}\xi)}{\mathrm{d}\xi} \xi \, \mathrm{d}\xi \tag{2.14}$$

and

$$\begin{aligned} \mathbf{M}_{ij} &= \frac{\partial^2}{\partial a_i \partial a_j} \left(\int_0^1 V^2 \xi \mathrm{d}\xi + \alpha V^2 \Big|_{\xi=\xi_o}\right) \\ &= \int_0^1 J_0(\lambda_{0,i}\xi) J_0(\lambda_{0,j}\xi) \xi \, \mathrm{d}\xi + \alpha J_0(\lambda_{0,i}\xi_o) J_0(\lambda_{0,j}\xi_o), \end{aligned} \tag{2.15}$$

where the dimensionless parameter α is defined as $\alpha = \Delta M/(2\pi m r_a^2)$, which physically indicates half of the ratio of the adsorbate mass to the total mass of the membrane.

The eigenvalue problem of equation (2.13) is formulated by the Rayleigh–Ritz method, whose accuracy is dependent on the accuracy of the deflection functions used to approximate the membrane mode shape. Instead of the Bessel functions, Timoshenko [51] used the following cosine functions to approximate the mode shape:

$$V(\xi) = a_1 \cos\left(\frac{\pi}{2}\xi\right) + a_2 \cos\left(\frac{3\pi}{2}\xi\right) + \cdots + a_i \cos\left[\frac{(2i-1)\pi}{2}\xi\right]. \tag{2.16}$$

The comparison of the first four $J_0(\lambda_{0,i}\xi)$ with $\cos[(2i-1)\pi\xi/2]$ is plotted in figure 3. Clearly, as seen in figure 3, when $i = 1$, the difference between $J_0(\lambda_{0,1}\xi)$ and $\cos(\pi\xi/2)$ is very small, which results in a 0.5% error in Timoshenko's first eigenfrequency computation compared with the exact one [51]. For $i = 2, 3$ and 4, the shape difference between $J_0(\lambda_{0,i}\xi)$ and $\cos[(2i-1)\pi\xi/2]$ enlarges significantly, which results in a much larger difference in the eigenfrequency computation. The same problem also appears when polynomials are used to approximate the mode shapes of the membrane [49]. Furthermore, even this 0.5% computation error of the first eigenfrequency is unacceptable in the micro/nano mass resonator application. One of the great advantages of the micro/nano mass resonator sensor is its ability to detect tiny fractional changes. For a nanoresonator with an eigenfrequency of gigahertz (10^9 Hz, GHz) or higher [11,12], this 0.5% difference means a megahertz (MHz) difference. As the exact mode shape of the Bessel function is used in our computations, equation (2.13) gives the exact values. For a nanoscaled mass resonator with a circular configuration, the Bessel functions must be used as the mode shapes.

3. Results and discussion

For axisymmetric excitation, the adsorbate mass and its location are the only two factors impacting the system eigenfrequencies. Here, the essential idea of using the two eigenfrequency changes to uniquely determine the adsorbate mass and location is based on the following

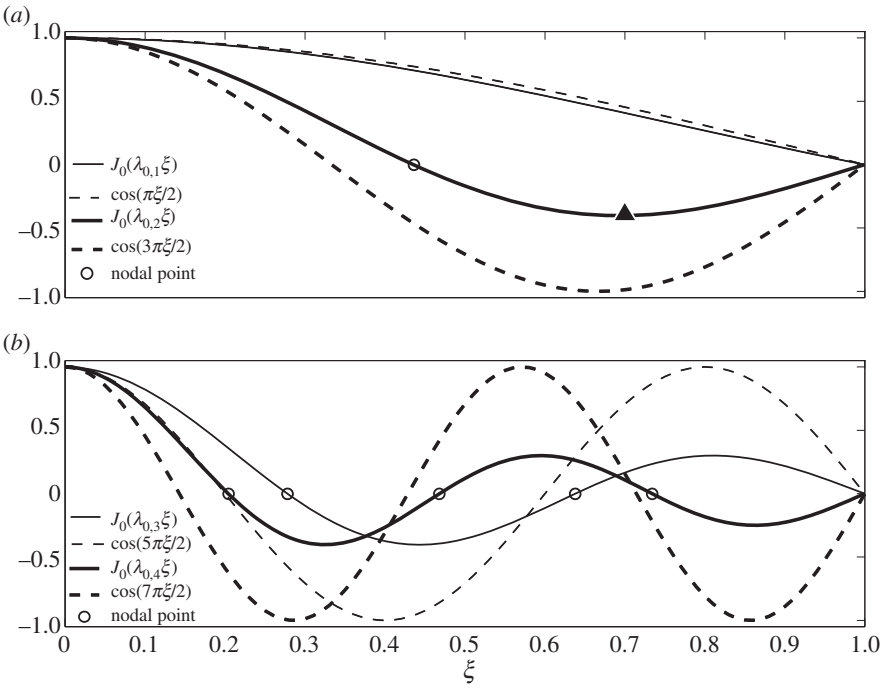

Figure 3. (*a*) Mode shapes of $J_0(\lambda_{0,1}\xi)$ and $J_0(\lambda_{0,2}\xi)$ in comparison with $\cos(\pi\xi/2)$ and $\cos(3\pi\xi)/2$. A solid triangle indicates the peak of $J_0(\lambda_{0,2}\xi)$. (*b*) Mode shapes of $J_0(\lambda_{0,3}\xi)$ and $J_0(\lambda_{0,4}\xi)$ in comparison with $\cos(5\pi\xi/2)$ and $\cos(7\pi\xi)/2$. The circles indicate the nodes.

fact: the response of different eigenfrequencies to the adsorbate mass and its location is different. Figure 4 plots the variations of the first (λ_1) and the second (λ_2) eigenfrequencies as the adsorbate moves from the centre towards the edge. In figure 4, α is fixed as $\alpha = 0.01$. λ_1 monotonically increases from 2.3112 at $\xi_o = 0$ to $\lambda_1 = \lambda_{0,1} = 2.4048$ at $\xi_o = 1$. In $0 \le \xi_o \le 0.44$, λ_2 monotonically increases from 4.9872 to $\lambda_2 = \lambda_{0,2} = 5.5201$, then in $0.44 \le \xi_o \le 0.7$, λ_2 monotonically decreases from 5.5201 to 5.4447, and finally in $0.7 \le \xi_o \le 1$, λ_2 monotonically increases from 5.4447 to 5.5201. These variations of λ_1 and λ_2 correspond exactly to the mode shape variation as given in figure 3. The magnitude of the first mode shape of $J_0(\lambda_{0,1}\xi)$ monotonically decreases from 1 to 0 as ξ changes from 0 to 1. The effect of adsorbate mass is thus largest at the centre and becomes zero at the edge. Therefore, λ_1 is minimum when the adsorbate is at the centre. When the adsorbate is at the edge, λ_1 recovers $\lambda_{0,1}$, which is the eigenfrequency of a membrane with no adsorbate. For the higher mode of $J_0(\lambda_{0,i}\xi)$ ($i \ge 2$), there are $i - 1$ nodes whose displacements are zero. When an adsorbate is at the nodes, the effective mass becomes zero and the eigenfrequency is thus unchanged. For the second mode of $J_0(\lambda_{0,2}\xi)$, there is one node at $\xi = \lambda_{0,1}/\lambda_{0,2} = 2.4048/5.5201 \approx 0.44$, which is marked as a circle in both figures 3 and 4. As seen in figure 3, $J_0(\lambda_{0,2}\xi)$ also has a peak at $\xi = 0.7$, which is marked as a solid triangle. The presence of a node and a peak is responsible for the λ_2 variation pattern as seen in figure 4.

Now let us present how to determine the adsorbate mass and its location by using the different responses of two eigenfrequencies. For $\alpha = 0.01$ and $\xi_o = 0.2$, the first two eigenfrequencies are uniquely determined by equation (2.13) as $\lambda_1 = 2.3273$ and $\lambda_2 = 5.2992$. In the real-world application of mass resonator sensors, the adsorbate mass (α) and its location (ξ_o) are the unknowns to be determined; the eigenfrequencies of λ_1 and λ_2 are the measured quantities. As a forward problem, once α and ξ_o are given, the eigenfrequencies are uniquely determined. However, as an inverse problem, there are infinite combinations of α and ξ_o that yield the same eigenfrequency for any single resonance mode. In figures 5 and 6, α is varied from 0 to 0.02

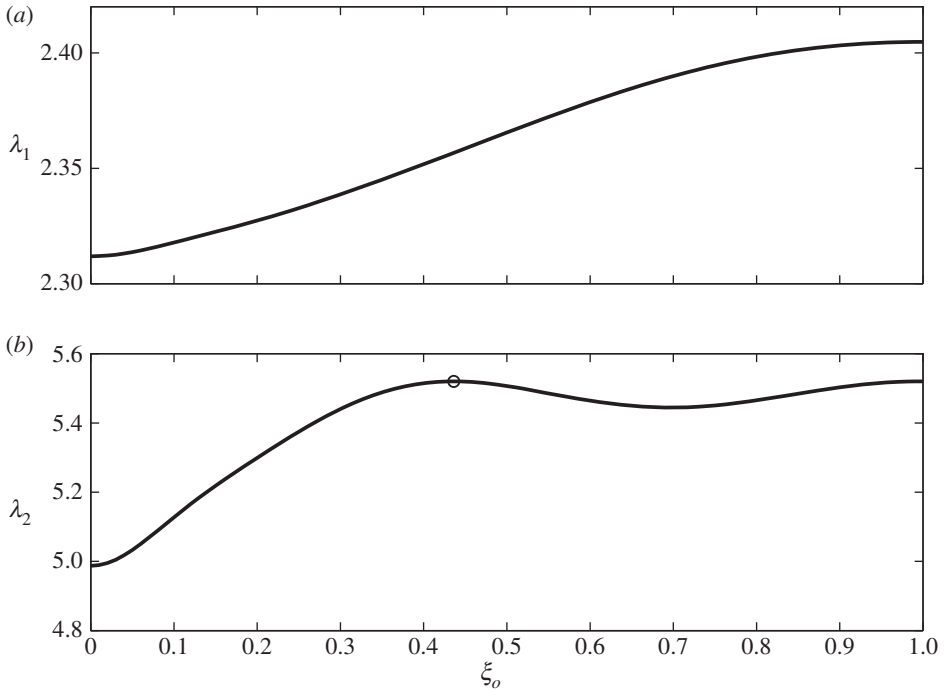

Figure 4. (*a*) Variation of the first resonance frequency (λ_1) as the adsorbate moves from the membrane centre towards the edge. (*b*) The corresponding variation of the second resonance frequency (λ_2). The circle corresponds to the node at which λ_2 has no changes. Here, the dimensionless concentrated mass is fixed as $\alpha = 0.01$.

with a step size of $\mathrm{d}\alpha = 4 \times 10^{-4}$ and ξ_o is varied from 0 to 1 with a step size of $\mathrm{d}\xi_o = 2 \times 10^{-2}$. Figure 5 plots the first eigenfrequency of λ_1 as a function of α and ξ_o. The level plane is the one with the fixed value of $\lambda_1 = 2.3273$. The intersection of the two planes is a curve, which physically indicates that there are infinite combinations of α and ξ_o resulting in the eigenfrequency of $\lambda_1 = 2.3273$. Figure 6 plots the second eigenfrequency of λ_2 as a function of α and ξ_o. The level plane is the one with the fixed value of $\lambda_2 = 5.2992$. Again, the intersection of the two planes is a curve, which is the infinite combinations of α and ξ_o resulting in the eigenfrequency of $\lambda_2 = 5.2992$. When the two intersecting curves obtained in figures 5 and 6 are projected into the $\alpha - \xi_o$ plane as shown in figure 7, there is an intersection marked as a circle, which happens to be exactly $(\alpha, \xi_o) = (0.01, 0.2)$. Again, the physical reason for the two curves to intersect is that the two eigenfrequencies have different responses to the adsorbate mass and its location. It is noteworthy that, even when an adsorbate lands on the nodal ring of the membrane, the above method can still work. Because only the axisymmetric modes are used, the position detected by the method is the radial position.

Equation (2.13) is for an undamped system, which has also been used to model many CNT and graphene resonators [14,16,30,31,42]. In reality, because the membrane energy dissipates, damping exists. With the presence of damping, the eigenvalue problem becomes the following:

$$\mathbf{K}G + \mathbf{D}\frac{\mathrm{d}\mathbf{G}}{\mathrm{d}t} + f\mathbf{M}\frac{\mathrm{d}^2\mathbf{G}}{\mathrm{d}t^2} = 0, \tag{3.1}$$

where the matrices $\mathbf{K}$ and $\mathbf{M}$ remain the same as those defined in equations (2.14) and (2.15); f is a constant defined as $f = mr_a^2/F$; $\mathbf{D}$ is the damping matrix defined as $\mathbf{D}_{ij} = (ca^2/F)\mathbf{M}_{ij}$ (c is the coefficient of damping [48]); $\mathbf{G}(t)$ is the vector associated with time-varying variables and defined as $\mathbf{G}^T(t) = (g_1(t), g_2(t), \ldots, g_n(t))$. Equation (3.1) is the so-called non-gyroscopic damped system [52], and the detailed computation procedure of finding its eigenvalues is presented in [6].

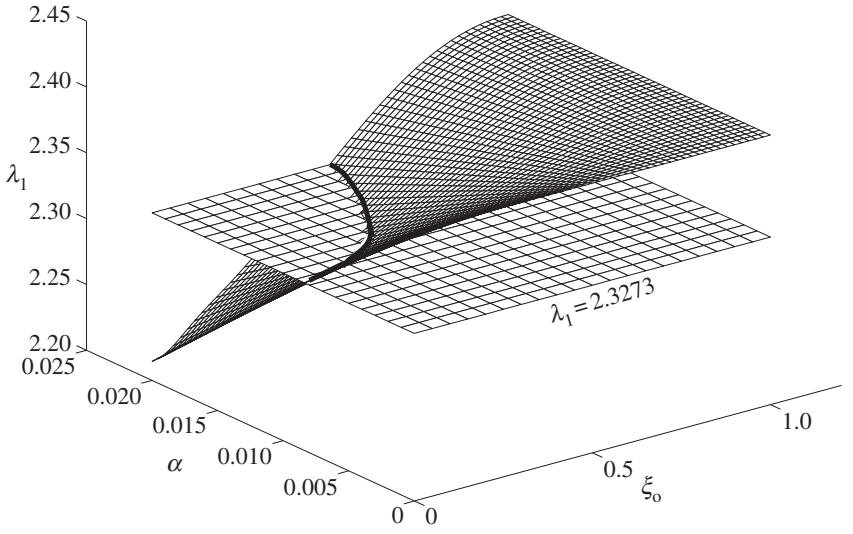

Figure 5. The λ_1 variation as a function of α and ξ_o. The level plane is the one with the constant of $\lambda_1 = 2.3273$. The intersection of the two planes is marked with a solid curve.

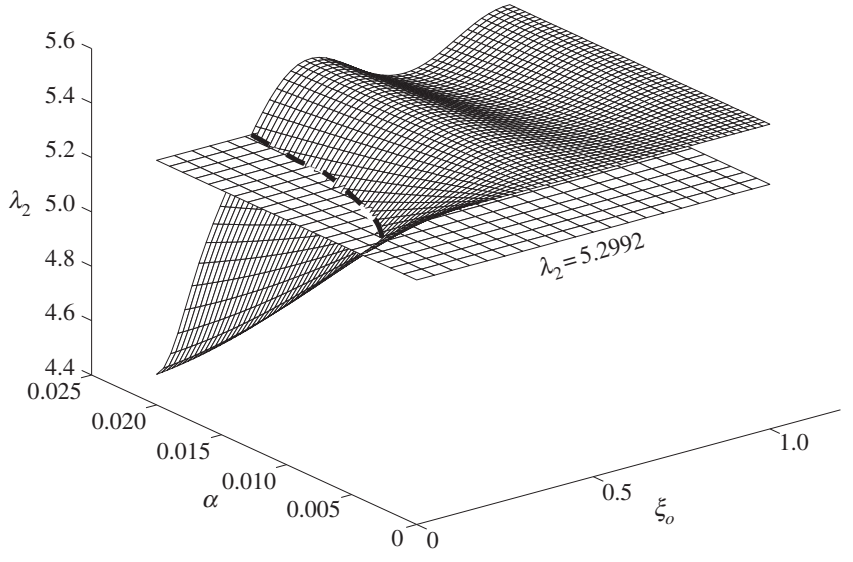

Figure 6. The λ_2 variation as a function of α and ξ_o. The level plane is the one with the constant of $\lambda_2 = 5.2992$. The intersection of the two planes is marked with a dashed curve.

The quality factor, Q, has the relationship of $Q \propto c^{-1}$. There are many studies for the damping mechanisms of small-scaled CNT and graphene resonators [18,19,22,27–29]. c is found by the so-called half-power method from the frequency response curve obtained from experiment [48], which is treated as a known parameter in equation (3.1). c is usually different in different mode and size-dependent [27–29]. The above method of using two resonant frequencies is also applicable to the non-gyroscopic damped system.

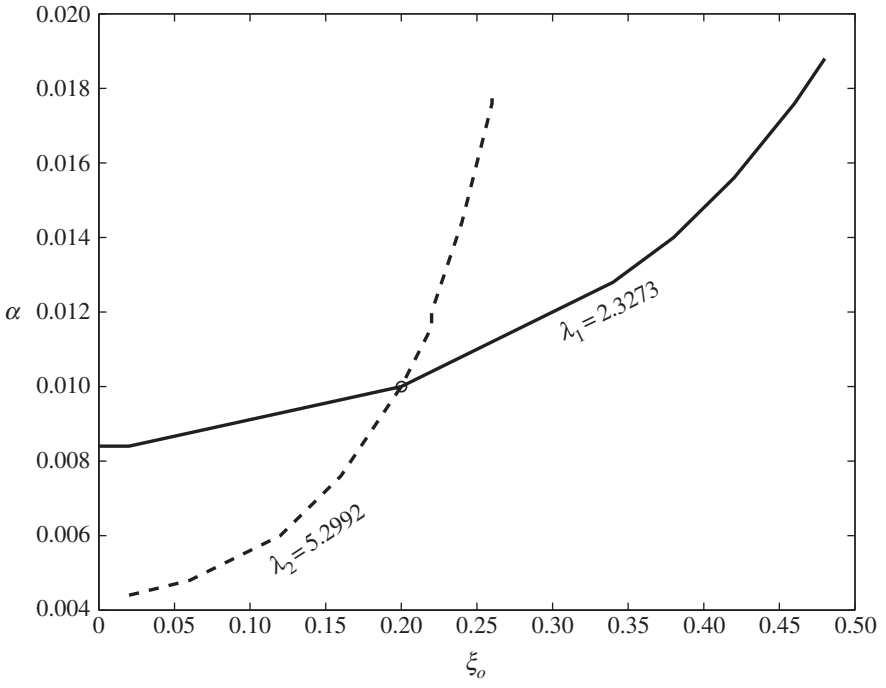

Figure 7. The projections of the two intersection curves obtained in figures 5 and 6 into the $\alpha - \xi_o$ plane. The intersection of the two curves is marked with a circle, which corresponds to $(\alpha, \xi_o) = (0.01, 0.2)$ exactly.

Because the model and method are developed for the one adsorbate case, we address the important issue of how to apply the method in a real experiment scenario. In the experiment, the previously adsorbed atoms/molecules/particles can be cleaned off by passing a large electric current through a resonator, which generates Joule heating and boils off the adsorbates [11]. However, it is impossible in a micro/nanomechanical mass resonator experiment to realize the scenario of just one adsorbate landing on a resonator during the spraying process. There are multiple adsorbates on a resonator surface [4,9–11,24]. When the number of adsorbates (N) is large and unknown, which usually is the case in a real experiment, our inverse problem-solving method can still apply in theory with much more complexity and much less efficiency. Furthermore, because the method requires $2N$ resonant frequencies to be measured to solve the inverse problem, it becomes much more difficult or even impossible in an experiment when N is large. Fortunately, in many micro/nanomechanical mass resonator applications, we do not have to solve the problem of multiple adsorbates. The underlying rationale is in the following three conditions. First, the state-of-art micro/nanomechanical resonators are so sensitive that they can detect the shifts in resonant frequencies induced by a single adsorption event. The step-wise decrease in resonant frequency recorded in the experiments indicates the discrete nature of adsorbates arriving at the micro/nanomechanical resonator surface one by one, which is also the hallmark of sensing the individual adsorption events of one protein [4,24], one atom [9,10] and one molecule [11]. By building a histogram of count versus frequency shift for the ensemble of sequential single gold atom adsorption, Jensen *et al.* [9] could identify with a certain confidence level that the gold atomic mass ranges between 0.1 and 1 zg compared with the true value of 0.327 zg ($1\,\text{zg} = 10^{-21}$ g). Similarly, by building histograms of event probability versus frequency shift for the ensembles of sequential single protein adsorption, Naik *et al.* [4] and Hanay *et al.* [24] could tell the masses of oligomers consisting of a 'nominally pure' bovine serum albumin protein and the different isoform masses of a human IgM antibody. Second, we need the assumption that the previously adsorbed particles have little or no impact on the step-wise decrease in resonant

frequency observed in the above experiments [4,9–11,24], the mass and position of an incoming particle being (solely) responsible for the decrease in resonant frequency. For the case of multiple (unknown) adsorbates, α in equation (2.15) becomes the following:

$$\alpha = \frac{\Delta M}{2\pi m r_a^2 + \sum_i^N M_i} \approx \frac{\Delta M}{2\pi m r_a^2}, \tag{3.2}$$

where N is the (unknown) number of previously adsorbed particles and M_i is the corresponding (unknown) mass; ΔM is the mass of an incoming particle. When the mass of adsorbates is much smaller than that of the resonator, i.e. $\sum_i^N M_i \ll \pi m r_a^2$, the approximation in equation (3.2) holds. As discussed above, one great advantage of micro/nanomechanical resonator sensors is that they can detect the tiny fractional shifts in resonant frequencies and very tiny masses can thus be sensed. In Chiu's experiment with noble gases as adsorbates [10], the mass of the CNT resonator is around 1000 zg, the atomic masses of xenon and argon are 0.218 zg and 0.066 zg, which corresponds to $\alpha = 1.09 \times 10^{-4}$ and $\alpha = 3.3 \times 10^{-5}$, respectively. In Hanay *et al.*'s experiment [24], α is around 10^{-4}. In these micro/nanomechanical mass resonator applications, the mass of the previously adsorbed particles has (almost) no impact on the resonant frequency, which is also an implicit assumption used in the above statistics methods [4,9,24]. The third condition is that there is enough time to measure the resonant frequencies between two individual adsorption events, which is why the step-wise decrease in resonant frequency can be monitored. As mentioned above, the resonant frequency of a micro/nanomechanical resonator can be as high as GHz or higher [11,12], the time required to measure the resonant frequency is thus very small. On the other hand, the adsorption rate is relatively slow, for example the argon adsorption rate is 0.09 atoms per second [10]. In conjunction with these three conditions, the inverse problem-solving method is viable in the real application of micro/nanomechanical mass resonators. The inverse problem-solving method also has the advantage of conducting mass sensing with just one datum of one single adsorption event. In the above statistics methods, tens or hundreds of data are needed to 'decouple' the two convolving parameters (mass and position of an adsorbate) by assuming a certain distribution rule such as Gaussian [4,9,24]. In contrast, our method can determine the mass and position of an adsorbate with one adsorption event.

4. Conclusion

The method of using two resonant frequencies to detect both the mass and position of an adsorbate on a circular membrane is presented. There are infinite combinations of the mass and its position which can result in the same resonant frequency shift. In this particular application, we show that using two resonant frequencies can uniquely and accurately determine the mass and its position. The two resonant frequencies used here are associated with the lowest two of the axisymmetric mode. As higher axisymmetric modes have higher resonant frequencies and thus better sensitivity, this method can be easily extended to this application scenario by simply calculating the other two different resonant frequencies. The non-axisymmetric modes, which make the theoretical and experimental analyses much more difficult, should be avoided in the drum resonator application. Only the mass effect of an adsorbate is considered by assuming very large in-plane tension. If the adsorbate-induced tension is considered, more resonant frequencies are needed to solve the inverse problem. The possibility of applying this inverse problem-solving method to the general/real scenario of multiple adsorbates in a micro/nanomechanical resonator experiment is also discussed.

Acknowledgements. The authors thank the anonymous reviewers for bringing up the issue of how to apply the model to a real application, which reshapes the presentation of this study.

Funding statement. The research was supported by the National Natural Science Foundation of China (NSFC nos 11023001 and 11372321).

References

1. Schedin F, Geim AK, Morozov SV, Hill EW, Blake P, Katsnelson MI, Novoselov KS. 2007 Detection of individual gas molecules adsorbed on graphene. *Nat. Mater.* **6**, 652–655. (doi:10.1038/nmat1967)
2. Cui Y, Wei Q, Park H, Lieber CM. 2001 Nanowire nanosensors for highly sensitive and selective detection of biological and chemical species. *Science* **293**, 1289–1292. (doi:10.1126/science.1062711)
3. Zijlstra P, Paulo PM, Orrit M. 2012 Optical detection of single non-absorbing molecules using the surface plasmon resonance of a gold nanorod. *Nat. Nanotechnol.* **7**, 379–382. (doi:10.1038/nnano.2012.51)
4. Naik AK, Hanay MS, Hiebert WK, Feng XL, Roukes ML. 2009 Towards single-molecule nanomechanical mass spectrometry. *Nat. Nanotechnol.* **4**, 445–450. (doi:10.1038/nnano.2009.152)
5. Ekinci KL, Yang YT, Roukes ML. 2004 Ultimate limits to inertial mass sensing based upon nanoelectromechanical systems. *J. Appl. Phys.* **95**, 2682–2689. (doi:10.1063/1.1642738)
6. Zhang Y, Murphy KD. 2011 Multi-modal analysis on the intermittent contact dynamics of atomic force microscope. *J. Sound Vib.* **330**, 5569–5582. (doi:10.1016/j.jsv.2011.07.018)
7. Bunch JS, van der Zande AM, Verbridge SS, Frank IW, Tanenbaum DM, Parpia JM, Craighead HG, McEuen PL. 2007 Electromechanical resonators from graphene sheets. *Science* **315**, 490–493. (doi:10.1126/science.1136836)
8. Zhang Y, Zhuo LJ, Zhao HS. 2013 Determining the effects of surface elasticity and surface stress by measuring the shifts of resonant frequencies. *Proc. R. Soc. A* **469**, 20130449. (doi:10.1098/rspa.2013.0449)
9. Jensen K, Kim K, Zettl A. 2008 An atomic-resolution nanomechanical mass sensor. *Nat. Nanotechnol.* **3**, 533–537. (doi:10.1038/nnano.2008.200)
10. Chiu H, Hung P, Postma H, Bockrath M. 2008 Atomic-scale mass sensing using carbon nanotube resonators. *Nano Lett.* **8**, 4342–4346. (doi:10.1021/nl802181c)
11. Chaste J, Eichler A, Moser J, Ceballos G, Rurali R, Bachtold A. 2012 A nanomechanical mass sensor with yoctogram resolution. *Nat. Nanotechnol.* **7**, 301–304. (doi:10.1038/nnano.2012.42)
12. Huang X, Zorman CA, Mehregany M, Roukes ML. 2003 Nanodevice motion at microwave frequencies. *Nature* **421**, 496. (doi:10.1038/421496a)
13. Knobel RG. 2008 Weighing single atoms with a nanotube. *Nat. Nanotechnol.* **3**, 525–526. (doi:10.1038/nnano.2008.250)
14. Bunch JS, Verbridge SS, Alden JS, van der Zande AM, Parpia JM, Craighead HG, McEuen PL. 2008 Impermeable atomic membranes from graphene sheets. *Nano Lett.* **8**, 2458–2462. (doi:10.1021/nl801457b)
15. Lee C, Wei X, Kysar JW, Hone J. 2008 Measurement of the elastic properties and intrinsic strength of monolayer graphene. *Science* **321**, 385–388. (doi:10.1126/science.1157996)
16. Garcia-Sanchez D, van der Zande AM, San Paulo A, Lassagne B, McEuen PL, Bachtold A. 2008 Imaging mechanical vibrations in suspended graphene sheets. *Nano Lett.* **8**, 1399–1403. (doi:10.1021/nl080201h)
17. Hiebert W. 2012 Devices reach single-proton limit. *Nat. Nanotechnol.* **7**, 278–280. (doi:10.1038/nnano.2012.66)
18. Kim SY, Park H. 2010 On the utility of vacancies and tensile strain-induced quality factor enhancement for mass sensing using graphene monolayers. *Nanotechnology* **21**, 105710. (doi:10.1088/0957-4484/21/10/105710)
19. Eichler A, Moser J, Chaste J, Zdrojek M, Wilson-Rae I, Bachtold A. 2011 Nonlinear damping in mechanical resonators made from carbon nanotubes and graphene. *Nat. Nanotechnol.* **6**, 339–342. (doi:10.1038/nnano.2011.71)
20. Lavrik NV, Sepaniak MJ, Datskos PG. 2004 Cantilever transducers as a platform for chemical and biological sensors. *Rev. Sci. Instrum.* **75**, 2229–2253. (doi:10.1063/1.1763252)
21. Mohanty P, Harrington DA, Ekinci KL, Yang YT, Murphy MJ, Roukes ML. 2002 Intrinsic dissipation in high-frequency micromechanical resonator. *Phys. Rev. B* **66**, 085416. (doi:10.1103/PhysRevB.66.085416)
22. Jöckel A, Rakher MR, Korppi M, Camerer S, Hunger D, Mader M, Treutlein P. 2011 Spectroscopy of mechanical dissipation in micro-mechanical membranes. *Appl. Phys. Lett.* **99**, 143109. (doi:10.1063/1.3646914)

23. Xia X, Li X. 2008 Resonance-mode effect on microcantilever mass-sensing performance in air. *Rev. Sci. Instrum.* **79**, 074301. (doi:10.1063/1.2949390)
24. Hanay MS, Kelber S, Naik AK, Chi D, Hentz S, Bullard EC, Colinet E, Duraffourg L, Roukes ML. 2012 Single-protein nanomechanical mass spectrometry in real time. *Nat. Nanotechnol.* **7**, 602–608. (doi:10.1038/nnano.2012.119)
25. Dohn S, Sandberg R, Svendsen W, Boisen A. 2005 Enhanced functionality of cantilever based mass sensors using higher mode. *Appl. Phys. Lett.* **86**, 233501. (doi:10.1063/1.1948521)
26. Burg T, Godin M, Knudsen SM, Shen W, Carlson G, Foster JS, Babcock K, Manalis SC. 2007 Weighing of biomolecules, single cells and single nanoparticle in fluid. *Nature* **446**, 1066–1069. (doi:10.1038/nature05741)
27. Adiga VP, Ilic B, Barton RA, Wilson-Rae I, Craighead HG, Parpia JM. 2011 Modal dependence of dissipation in silicon nitride drum resonators. *Appl. Phys. Lett.* **99**, 253103. (doi:10.1063/1.3671150)
28. Adiga VP, Ilic B, Barton RA, Wilson-Rae I, Craighead HG, Parpia JM. 2012 Approaching intrinsic performance in ultra-thin silicon nitride drum resonators. *J. Appl. Phys.* **112**, 064323. (doi:10.1063/1.4754576)
29. Barton RA, Ilic B, van der Zande AM, Whitney WS, McEuen PL, Parpia JM, Craighead HG. 2011 High, size-dependent quality factor in an array of graphene mechanical resonators. *Nano Lett.* **11**, 1232–1236. (doi:10.1021/nl1042227)
30. Li C, Chou T. 2004 Mass detection using carbon nanotube-based nanomechanical resonators. *Appl. Phys. Lett.* **84**, 5246–5248. (doi:10.1063/1.1764933)
31. Dai M, Kim C, Eom K. 2012 Nonlinear vibration behavior of graphene resonator and their applications in sensitive detection. *Nanoscale Res. Lett.* **7**, 499. (doi:10.1186/1556-276X-7-499)
32. Zhang Y. 2011 Eigenfrequency computation of beam/plate carrying concentrated mass/spring. *J. Vib. Acoust.* **133**, 021006. (doi:10.1115/1.4002121)
33. Wu JS, Luo SS. 1997 Use of the analytical and numerical combined method in the free vibration analysis of a rectangular plate with any number of point masses and translational springs. *J. Sound Vib.* **200**, 179–194. (doi:10.1006/jsvi.1996.0697)
34. Chai GB. 1995 Frequency analysis of a S-C-S-C plate carrying a concentrated mass. *J. Sound Vib.* **179**, 70–177. (doi:10.1006/jsvi.1995.0011)
35. Zhang Y. 2013 Determining the adsorption-induced surface stress and mass by measuring the shifts of resonant frequencies. *Sens. Actuators A* **194**, 169–175. (doi:10.1016/j.sna.2013.01.029)
36. Dohn S, Svendsen W, Boisen A, Hansen O. 2007 Mass and position determination of attached particles on cantilever based mass sensors. *Rev. Sci. Instrum.* **78**, 103303. (doi:10.1063/1.2804074)
37. Wei Y, Wang B, Wu J, Yang R, Dunn ML. 2013 Bending rigidity and Gaussian stiffness of single-layered graphene. *Nano Lett.* **13**, 26–30. (doi:10.1021/nl303168w)
38. Atalaya J, Isacsson A, Kinaret JM. 2008 Continuum elastic modeling of graphene resonators. *Nano Lett.* **8**, 4196–4200. (doi:10.1021/nl801733d)
39. Komaragiri U, Begley MR, Simmons JG. 2005 The mechanical response of freestanding circular elastic films under point and pressure loads. *J. Appl. Mech.* **72**, 203–212. (doi:10.1115/1.1827246)
40. Koenig SP, Boddeti NG, Dunn ML, Bunch JS. 2011 Ultrastrong adhesion of graphene membrane. *Nat. Nanotechnol.* **6**, 543–546. (doi:10.1038/nnano.2011.123)
41. Bao W, Miao F, Chen Z, Zhang H, Jang W, Dames C, Lau C. 2009 Controlled ripple texturing of suspended graphene and ultrathin graphite membranes. *Nat. Nanotechnol.* **4**, 562–566. (doi:10.1038/nnano.2009.191)
42. Chen C, Rosenblatt S, Bolotin KI, Kalb W, Kim P, Kymissis I, Stormer HL, Heinz TF, Hone J. 2009 Performance of monolayer graphene nanomechanical resonators with electrical readout. *Nat. Nanotechnol.* **4**, 861–867. (doi:10.1038/nnano.2009.267)
43. Chi M, Zhao YP. 2009 Adsorption of formaldehyde molecule on the intrinsic and Al-doped graphene: a first principle study. *Comput. Mater. Sci.* **46**, 1085–1090. (doi:10.1016/j.commatsci.2009.05.017)
44. Chi M, Zhao YP. 2012 First principle study of the interaction and charge transfer between graphene and organic molecules. *Comput. Mater. Sci.* **56**, 79–84. (doi:10.1016/j.commatsci.2011.12.035)
45. Zhang Y. 2010 Extracting nanobelt mechanical properties from nanoindentation. *J. Appl. Phys.* **107**, 123518. (doi:10.1063/1.3432748)

46. Chopin J, Vella D, Boudaoud A. 2008 The liquid blister test. *Proc. R. Soc. A* **464**, 2887–2906. (doi:10.1098/rspa.2008.0095)
47. Courant R, Hilbert D. 1961 *Methods of mathematical physics*, vol. 1. New York, NY: Interscience.
48. Meirovitch L. 1967 *Analytical methods in vibrations*. New York, NY: Macmillan Publishing Co. Inc.
49. Sagan H. 1989 *Boundary and eigenvalue problems in mathematical physics*. New York, NY: Dover Publications Inc.
50. McLachlan NW. 1955 *Bessel functions for engineers*, 2nd edn. London, UK: Oxford University Press.
51. Timoshenko SP. 1937 *Vibration problems in engineering*, 2nd edn. New York, NY: van Nostrand.
52. Meirovitch L. 1980 *Computational methods in structural dynamics*. Rockville, MD: Sijthoff & Noordhoff Inc.